Petroleum Science 22 (2025) 805–820

Contents lists available at ScienceDirect

Petroleum Science

journal homepage: www.keaipublishing.com/en/journals/petroleum-science

Original Paper

Novel dual-enhanced stimulation for safe and efficient marine hydrate production

Yun Qi [a, b], You-Hong Sun [a, b], Bing Li [a, b, *], Heng-Feng Shan [a, b], Yi-Zhuo Liu [a, b], Guo-Biao Zhang [a, b, **]

[a] *School of Engineering and Technology, China University of Geosciences, Beijing, 100083, China*
[b] *Key Laboratory of Polar Geology and Marine Mineral Resources (China University of Geosciences, Beijing), Ministry of Education, Beijing, 100083, China*

ARTICLE INFO

Article history:
Received 27 June 2024
Received in revised form
12 November 2024
Accepted 12 November 2024
Available online 14 November 2024

Edited by Yan-Hua Sun

Keywords:
Natural gas hydrate
Dual-enhanced stimulation
Splitting grouting
Hydrate production
Pore structure

ABSTRACT

The commercial exploitation of natural gas hydrates is currently facing several challenges, including low production rates, limited recovery areas, and brief periods of continuous production. To address these issues, we propose a novel dual-enhanced stimulation (DES) method for marine hydrate reservoirs. This method involves injecting a special slurry that solidifies into porous, high-permeability, and high-strength slurry veins. These veins not only enhance permeability, allowing for faster gas and water flow, but also improve reservoir stability. This study experimentally investigated the split grouting of clayey-silty sediments with dual-enhanced slurry to assess the feasibility of DES and to explore the slurry diffusion mechanism and micro-pore structure of the veins. The results showed that split grouting with dual-enhanced slurry exhibited frequent fracture initiation with quick pressure spikes and sharp declines, suggesting shorter fractures in clayey-silty sediments. As vertical stress increased, the primary diffusion direction of the dual-enhanced slurry shifted from horizontal to vertical, aligning with fracture propagation patterns observed during fracturing. Unlike hydraulic fracturing in hard rocks, split grouting in clayey-silty sediments encountered more difficult conditions. These veins formed through a recurring cycle of splitting into fractures and filling with slurry, occurring more frequently in weaker sediments with slower injection rates and higher vertical stress. Increased vertical stress hindered slurry vein diffusion, easily resulting in compaction grouting near the grouting pipe. Additionally, three-dimensional laser scanning of the veins showed that those formed through split grouting were continuous and stable, with their thickness decreasing as diffusion distance increased. The morphology of these veins was shaped by factors such as grouting rate, formation stress, and elastic modulus, with higher rates and elastic moduli facilitating the formation of complex vein networks. Mercury intrusion porosimetry demonstrated that the DES method resulted in veins with consistent effective porosity between 65% and 70% and median pore sizes of 11–15 μm across different locations. These veins formed a well-connected porous network of smaller pores, significantly enhancing both permeability and sand control. The research findings validate the effectiveness of the DES method for marine hydrate reservoirs, providing a strategy for the safe and efficient exploitation of NGH resources.

1. Introduction

Natural gas hydrate (NGH), primarily composed of methane and water, forms under specific conditions of low temperature and high pressure. This substance is seen as a potential alternative energy source due to its high energy potential and vast reserves (Collett, 2002; Max, 2003; Sloan Jr and Koh, 2007). The main techniques recognized globally for extracting NGH include depressurization, thermal stimulation, and carbon dioxide replacement, along with various combinations of these methods (Moridis and Collett, 2003; Sun et al., 2019b). Depressurization, in particular, is regarded as the most effective strategy for industrial-scale pilot production of NGH, especially in offshore settings. This was evidenced in the NGH production trials conducted in the South China Sea in 2017 and 2020, where depressurization was utilized (Li et al., 2018a; Ye et al., 2020). However, challenges such as the low permeability and

---

* Corresponding author.
** Corresponding author.
E-mail addresses: bing@cugb.edu.cn (B. Li), zhanggb@cugb.edu.cn (G.-B. Zhang).

https://doi.org/10.1016/j.petsci.2024.11.010

mechanical strength of the reservoir were identified as significant hurdles to efficient production, suggesting that reservoir stimulation is essential for the commercial viability of NGH extraction.

Hydraulic fracturing technology enhances reservoir permeability by creating a complex network of fractures through high-pressure injection of fracturing fluid into the reservoir, which is widely used in conventional oil and gas reservoirs. Konno et al. (2016), Too et al. (2018), Wang et al. (2023), Yang et al. (2020), Ma et al. (2022) and Zhang et al. (2020b) have proven through hydraulic fracturing experiments that hydrate-bearing sediments can be fractured, observing a subsequent increase in sediment permeability. Moreover, Chen et al. (2017), Sun et al. (2019a), Li et al. (2021a), Liu et al. (2023), and Feng et al. (2019), through numerous numerical simulations under the assumption of constant fracture conductivity, have shown that hydraulic fracturing can enhance the efficiency of NGH production.

The use of hydraulic fracturing technology to enhance reservoir permeability is considered to be an important technical means of improving NGH extraction efficiency. In addition to hydraulic fracturing technology, some scholars have proposed several methods for the stimulation of NGH reservoirs. Wang et al. (2018b) proposed enhancing gas production by promoting hydrate decomposition through the injection of hot fluids. Li et al. (2020) suggested improving gas hydrate reservoir extraction efficiency by injecting foam slurries into the reservoir to establish high-permeability channels, with numerical simulation results indicating that this technique significantly increases reservoir permeability and methane production. Zhang et al. (2019a) proposed the method of increasing methane production by enlarging the high-permeability wellbore. However, due to the weakly cemented and unconsolidated nature of marine gas hydrate reservoirs (Yun et al., 2007; Boswell and Collett, 2011; Li et al., 2018a; You et al., 2019; Ma et al., 2021), the application of conventional reservoir stimulation methods in NGH reservoirs has certain limitations. With the decomposition of hydrate, the strength and stiffness of the reservoir will decrease, while its plasticity will increase. In addition, the decomposition of hydrate is accompanied by heat and mass transfer, phase transformation, and multiphase seepage, which are also contributing factors to reservoir creep (Chen et al., 2023; Li et al., 2023). Under the combined influence of these two factors, the proppant will inevitably become embedded in the reservoir, leading to support failure (Hayashi and Haimson, 2012). Thermal fluid injection does not effectively enhance reservoir permeability or production range. Other reservoir stimulation methods may also encounter issues like sand production and reservoir instability, which compromise long-term stable extraction.

Given the distinctive geological and mechanical characteristics of NGH reservoirs in the South China Sea, we propose a dual-enhanced stimulation (DES) method, as shown in Fig. 1. This approach involves injecting a specially formulated slurry into the NGH reservoir to establish a robust, highly permeable network of slurry veins. These veins fulfill two key roles: they act as efficient conduits for rapid flow of gas and water, thereby improving reservoir permeability, and they also reinforce the geological structure, enhancing the overall stability of the reservoir. Our previous work (Sun et al., 2022) has developed a dual-enhanced slurry specifically designed for NGH reservoirs. This innovative slurry, formulated from polyurethane-based chemical grout, is capable of curing at low temperatures (5–15 °C), resulting in a solidified structure characterized by exceptional pore interconnectivity and notable strength. The resulting porous medium, formed after the dual-enhanced slurry solidifies, can achieve a permeability exceeding 5 D, along with compressive strengths ranging between 9 and 19 MPa.

The splitting grouting can be used to inject dual-enhanced slurry into the NGH reservoirs to form a complex network of slurry veins, which had been widely applied in reservoir sealing and soft soil foundation reinforcement (Wang et al., 2018a; Guo et al., 2019). It involves the injection of slurry into the foundation or reservoir under high pressure, with the diffusion distance and range of the slurry being important evaluation criteria for the grouting effectiveness (Draganović and Stille, 2011). Studies have shown that the diffusion of slurry in the strata depends on the grouting conditions, properties of the slurry, and physicochemical characteristics of the foundation or reservoir (Gustafson and Stille, 1996; Saeidi et al., 2013). Hao et al. (2023) described the polymer directional splitting grouting process in four stages: filling, extrusion, split-extrusion cycle, and final extrusion. They noted that factors such as the shape of the grouting hole, grouting volume and rate, and the soil's elastic modulus and cohesion affect the diffusion shape of polymer grouting materials. Guo et al. (2019) observed that injecting polyurethane foam into the soil leads to vertical fractures, with material spreading unevenly due to soil variability. Niu et al. (2020) identified three types of grouting veins in soils: trunk grouting veins, branch grouting veins, and permeable filling grouting veins, highlighting that the veins' thickness decreases with distance from the injection point. Li et al. (2018b) found that in less permeable soils, grouting results in the formation of three vein types: skeleton-supporting veins, intersecting grid veins, and parallel dispersed veins, with their thickness decreasing and their orientation becoming more random farther from the injection site.

These studies collectively demonstrate that splitting grouting technology can create a complex network of slurry veins in weak soil and further illustrate the theoretical feasibility of applying this technology for the DES of NGH reservoirs, with the formation of these slurry vein networks influenced by various factors. However, the weakly cemented and low-strength characteristics of marine clayey-silty NGH reservoirs (Ye et al., 2020), which differ markedly from conventional reservoirs in terms of mechanical properties, present various challenges. Notably, the distinctive features of these weak clayey-silty NGH reservoirs make the process of injecting dual-enhanced slurry, which leads to splitting and the complex formation of porous slurry veins, quite complicated. Additionally, the diffusion and pore structure of the slurry veins remain unclear.

Therefore, this study conducted splitting grouting experiments to validate the feasibility of DES in clayey-silty NGH reservoirs. The dynamic diffusion characteristics of the slurry veins were analyzed by examining the variations in grouting pressure and formation stress during the grouting process. Subsequently, three-dimensional laser scanning was conducted on the excavated slurry veins to determine their morphology, dimensions, and the area of reservoir stimulation. Finally, mercury injection tests were performed on the slurry veins at different locations to investigate the influence of diffusion distance on porosity and pore structure of slurry veins. This research introduces an innovative DES method for marine NGH reservoirs, offering a pathway to secure and effective development of NGH resources.

2. Experimental

2.1. Experimental apparatus

As depicted in Fig. 2, the experimental setup for split grouting includes three main systems: grouting, reservoir simulation, and data acquisition. The grouting system features a pump capable of maintaining constant pressure and flow up to 30 MPa, a high-pressure hose, a grouting pipe, and two high-pressure piston containers with volumes of 1 and 2 L, each designed to withstand a maximum pressure of 25 MPa. The high-pressure hose, made of

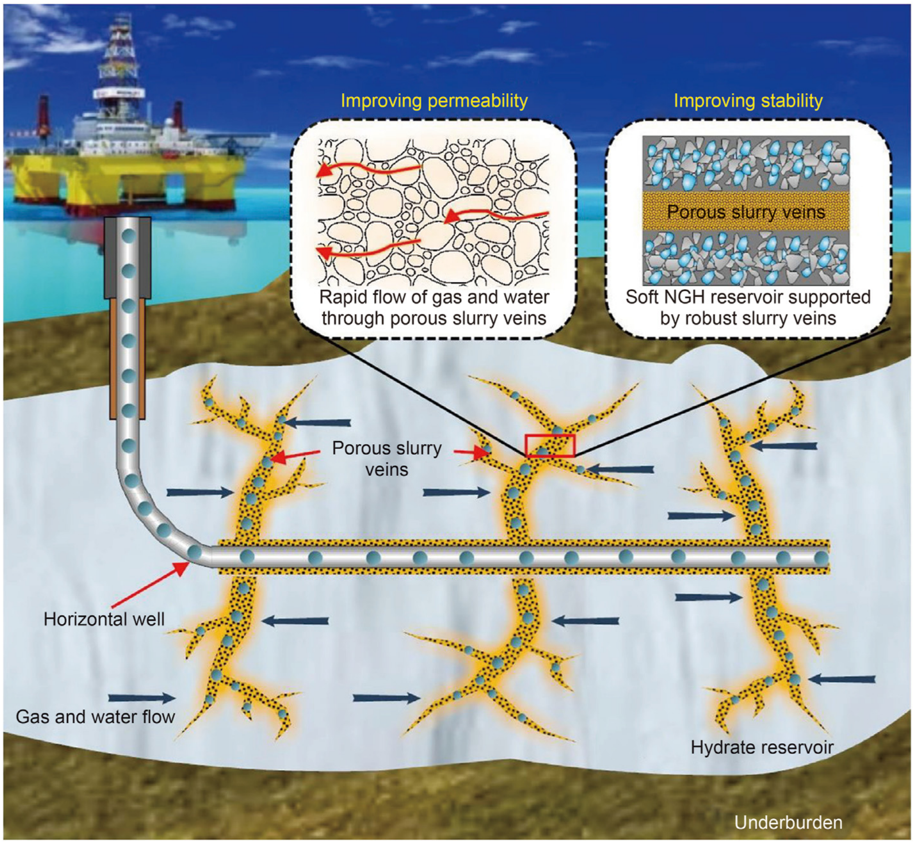

Fig. 1. The schematic diagram of the dual-enhanced stimulation method for marine NGH reservoirs.

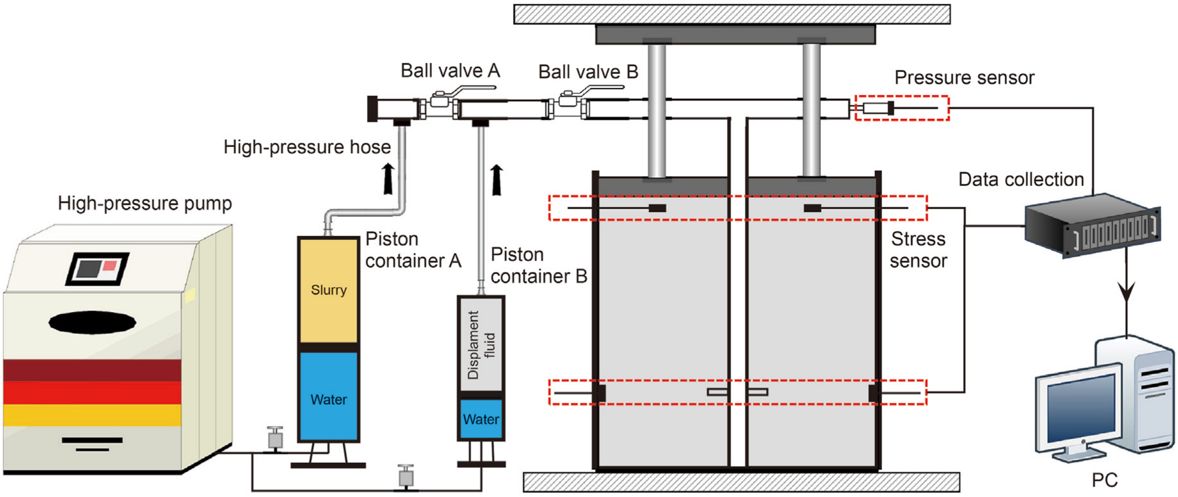

Fig. 2. Schematic diagram of splitting grouting experimental apparatus.

multi-layered steel wire rubber, is tailored for slurry transport and can endure up to 20 MPa. The grouting pipe, which is 400 mm tall with a 10 mm internal diameter, has several exterior grooves to increase the contact area with the sediment. Directly below the grouting pipe, two symmetrically aligned grouting holes, each 7 mm in diameter and 10 mm long, allow for the slurry's entry into the sediments. The reservoir simulation system comprises a reaction frame, a cylindrical reactor (300 mm in diameter and 350 mm high) for containing the sediment, and a sample press disc to compact the sediment and apply vertical ground stress. The data acquisition system includes a pressure sensor to monitor changes in the grouting pipe's pressure, a stress sensor to observe ground stress variations during grout diffusion, and a data acquisition module and computer for real-time data collection and analysis.

2.2. Experimental materials

This study targets recreating the clayey-silty sediment composition from the first NGH production test area in the South China Sea, with a blend mirroring the observed mix of 53% quartz feldspathic, 16% carbonates, and 26%–30% clay minerals (notably montmorillonite and illite) (Li et al., 2018a). The selected proportions for simulating these sediments involve combining 1000 mesh quartz sand, carbonate, illite, and montmorillonite in a ratio of 0.54:0.16:0.20:0.10. The study utilizes an experimental slurry made from polyurethane, presenting as a brown-yellow multiphase mixture with a density of 1.68 g/cm^3. Initially, the slurry has a viscosity of 460 mPa·s, which can be reduced to 50 mPa·s with the addition of a 10% viscosity reducer, making it comparable to the guar gum fracturing fluid in hydraulic fracturing (Fink, 2021), thus fitting the injection needs. The rheological curve of dual-enhanced slurry at 20 °C and its consolidated body are shown in Fig. 3. As the shear rate increases, the shear stress also shows an increasing trend. The consolidated body demonstrates a permeability of 5.75 μm^2, with a consistent pore distribution and effective connectivity, and a compressive strength ranging from 9 to 19 MPa under confining pressures of 4–10 MPa. Key physical properties of the slurry are detailed in Table 1, with additional information on slurry properties and experimental approaches available in previous publication (Sun et al., 2022).

2.3. Experimental procedure

2.3.1. Sediment preparation

In the experiments, a specific amount of deionized water was mixed with the sediments in accordance with the water saturation and porosity found in the clayey-silty hydrate reservoirs of the Shenhu Area. This mixture was incrementally transferred to the reactor and methodically compacted to reach the desired porosity and water saturation levels of 45% and 60%. Due to the extensive number of sediment samples, this filling and compaction process was repeated multiple times for each sample to guarantee even compaction. During this phase, stress sensors and a steel grouting pipe were buried within the sediments. For experiments involving frozen sediments, the reactor containing the samples was placed in a freezer at −15 °C. After 24 h, the frozen samples were promptly removed for the grouting experiments. Recognizing the significant impact of reservoir mechanical properties on fracture propagation, triaxial compression tests were conducted on two types of sediment samples (frozen and unfrozen sediments) to determine their mechanical properties, with the results presented in Fig. 4.

Using Mohr stress circle analysis, we ascertained that the cohesive strength and internal friction angle of unfrozen sediments are 400 kPa and 29°, respectively. Remarkably, these properties align well with those observed in hydrate-free sediments from the South China Sea, reported to be 151 kPa and 34° (Li et al., 2021c). In the case of sediments with a 60% ice saturation, cohesion and internal friction angles were determined to be 756 kPa and 31°. When compared to hydrate-bearing sediments with 30% saturation, exhibiting 322 kPa and 31° (Li et al., 2021c), it is evident that, aside from higher cohesion, the internal friction angles are consistent. In addition, the elastic modulus between different sediments was compared, and the results are shown in Fig. 5. By comparison, it was found that the elastic modulus of frozen sediment and hydrate-containing sediment is close to 500 MPa when the confining pressure is 1 MPa, which is higher than that of non-frozen sediment and non-hydrate-containing sediment. This consistency significantly underscores the experimental results' applicability.

2.3.2. Dual-enhanced slurry prepared

The concoction of the dual-enhanced slurry is comprised of base liquids A and B, along with pore-forming agents, reaction control agents, enhancers, and viscosity reducers. Initially, base liquid B, the pore-forming agent, reaction control agent, enhancer, and viscosity reducer were precisely measured and deposited into the mixing container. A dual-axis high-speed mixer with adjustable speed was activated at 1000 rpm to ensure that the components were thoroughly blended. Following this step, a predetermined quantity of base liquid A was added to the mixture and stirred until it reached a homogenous state. This freshly prepared slurry was then poured into high-pressure piston container A. Parallel to this, oil-based liquid, used as the displacement fluid, was introduced into high-pressure piston container B. To align with the capacity of the reactor, the grouting volume was maintained at a moderate level, with a consistent injection volume of 1 L for all the experimental groups.

2.3.3. Dual-enhanced stimulation of clayey-silty sediments

The prepared sediment sample, housed within the reactor, was mounted on a reaction frame and subjected to vertical ground stress via a hydraulic press. Once the ground stress stabilized, slurry

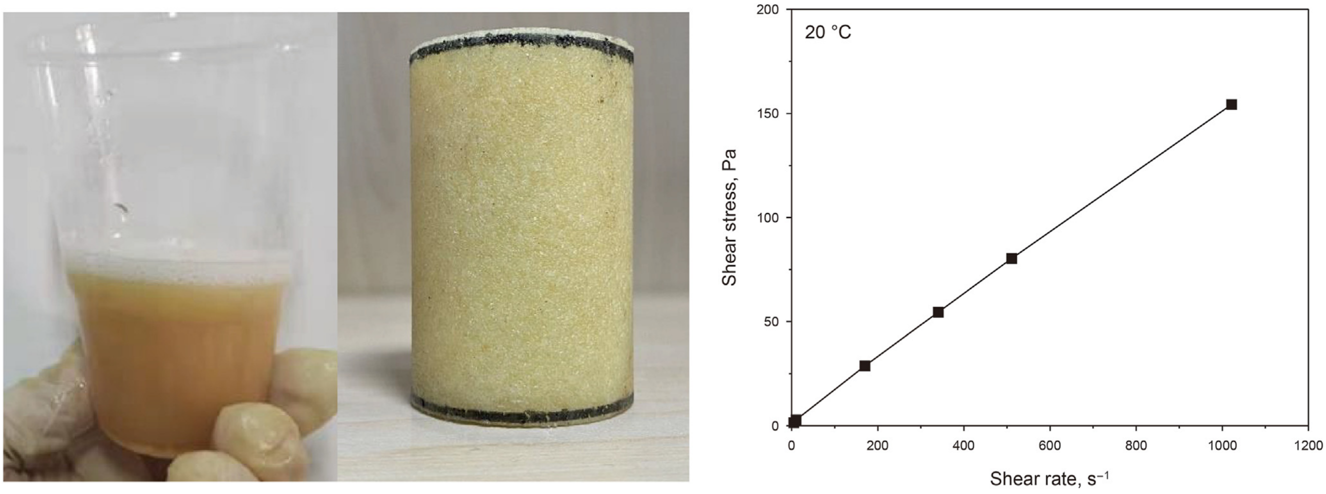

Fig. 3. Dual-enhanced slurry and its rheological curve and consolidated body.

Table 1
Main physical properties of dual-enhanced slurry.

Appearance	Density @ 20 °C, g/cm^3	Viscosity @ 20 °C, mPa·s	Initial curing time @ 10 °C, min	Full curing time @ 10 °C, h
Brown-yellow liquid	1.68	50–460	30–360	18–24

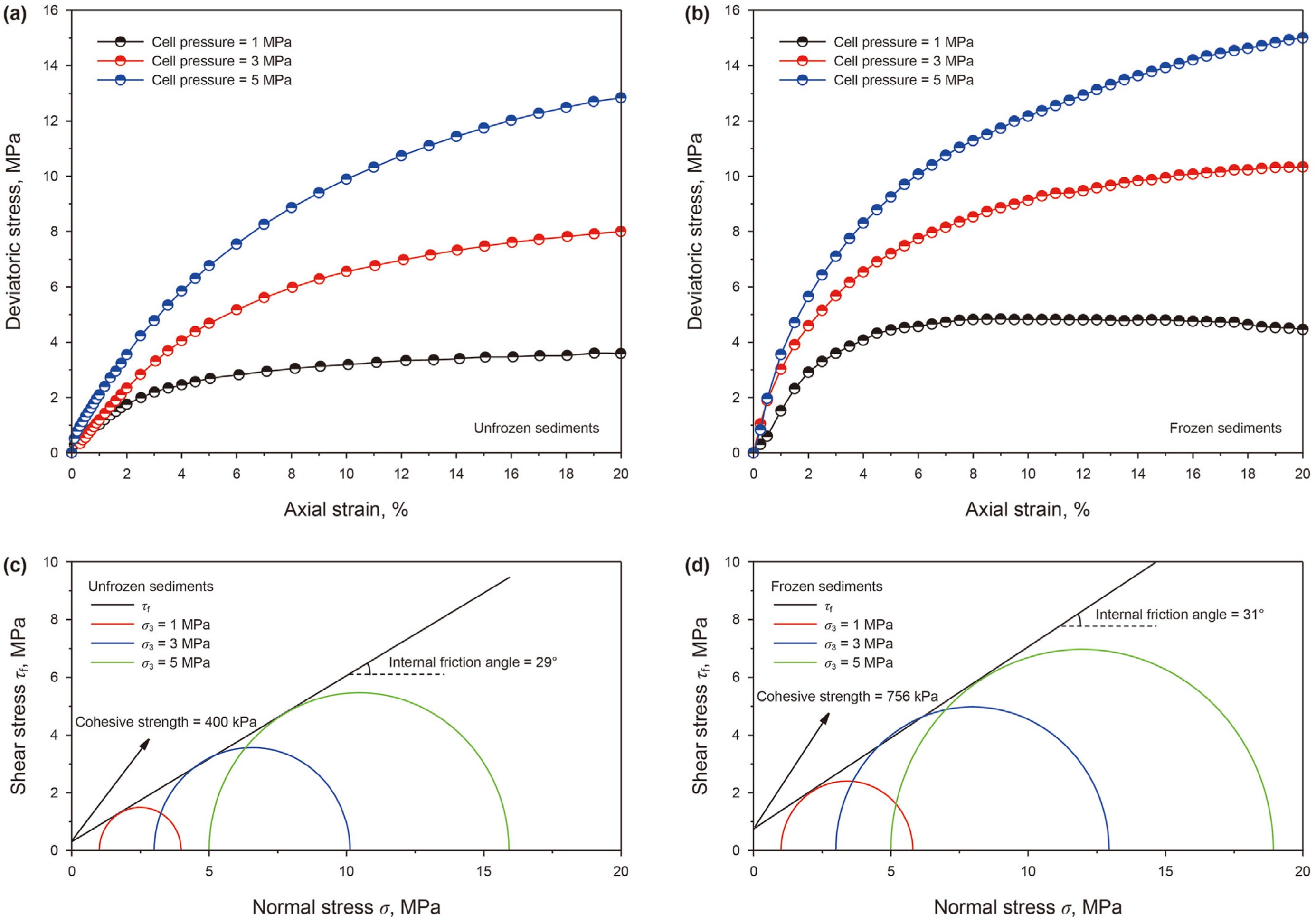

Fig. 4. Triaxial mechanical strength and Mohr stress circle of sediments (σ_3 is the confining pressure).

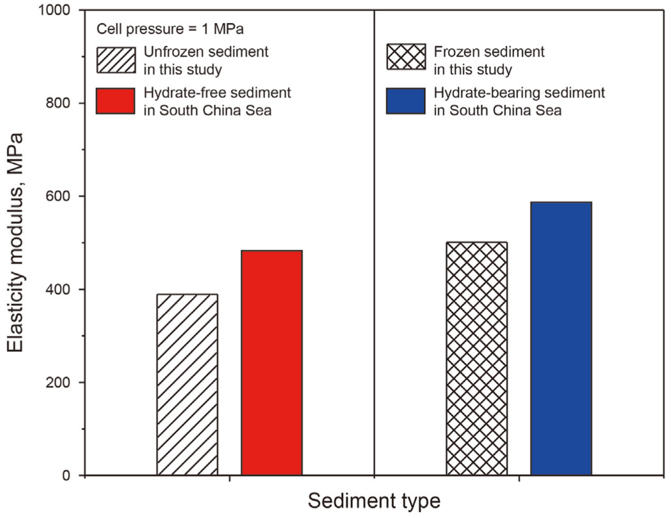

Fig. 5. The elastic modulus of different types of sediments.

injection commenced at a uniform flow rate. Continuous pressure monitoring within the grouting pipe was conducted to assess the slurry's dynamic diffusion into the sediment layers. Ground stress and flow rate were also tracked in real-time throughout the injection phase. Following the complete injection of the slurry, a steady flow of a displacement fluid was employed to ensure the slurry was fully transferred from the grouting pipe into the sediment layers. In this study, the viscosity of the dual-enhanced slurry was 300 mPa·s. After grouting, the slurry is allowed to cure inside the reactor for 24 h at 20 °C before the slurry veins are excavated. To explore the effects of varying grouting rates, vertical ground stress, and the sediment's mechanical characteristics on the formation and propagation of slurry veins, a total of twelve experiments were conducted. Table 2 contains the comprehensive details of the various grouting protocols. Additionally, certain experimental groups were repeated to ensure the consistency and validity of the results obtained.

2.3.4. *Measurements of slurry vein morphology and pore structure*

Following the completion of the split grouting process, a curing

Table 2
Experimental parameters for dual-enhanced stimulation of clayey-silty sediments.

Run	Properties of sediment			Vertical ground stress, kPa	Grouting rate, mL/min
	Porosity, %	Water saturation, %	Frozen sediment		
1	42	60	No	0	100
2-1	42	60	No	200	100
2-2	42	60	No	200	100
3	42	60	No	200	150
4-1	42	60	No	200	200
4-2	42	60	No	200	200
5-1	42	60	No	400	100
5-2	42	60	No	400	100
6	42	60	Yes	400	100
7-1	42	60	No	400	200
7-2	42	60	No	400	200
8	42	60	Yes	400	200
9	42	60	No	600	100
10	42	60	No	600	200
11	42	60	Yes	600	200
12-1	42	60	No	600	300
12-2	42	60	No	600	300

period of 24 h was allowed for the slurry to harden completely. After the curing period, a sampling shovel was employed to carefully excavate the sediments to retrieve the slurry veins. The extracted slurry veins then underwent geometric measurement using three-dimensional laser scanning technology. For ascertaining the effective coverage of the DES, the cumulative surface area of the slurry veins was calculated and marked as the area of stimulation.

To further analyze the impact of the stimulation on formation permeability, samples of the slurry veins were collected at various distances from the grouting pipe and subjected to mercury intrusion porosimetry. This analysis, which provided detailed information on porosity and pore size distribution, aimed to elucidate how the slurry veins contribute to the overall enhancement of the formation's permeability.

3. Results and discussion

3.1. Dynamic diffusion characteristics of slurry veins

To investigate the diffusion behavior of slurry veins within the reservoir, this study monitored variations in formation stress and grouting pressure. The dynamics of slurry vein splitting and their subsequent spread within the reservoir were deduced from the observed changes in grouting pressure. As the slurry flowed into the reservoir, it applied pressure on the surrounding sediments, which resulted in deformation and consequent shifts in formation stress. To capture these shifts accurately, four stress sensors were installed in key locations: along the axis of perforation and perpendicular to it, to map the stress distribution. And two sensors were placed in the upper part of the reservoir to monitor the variations in vertical stress. The data gathered from these sensors were instrumental in pinpointing the predominant direction in which the slurry veins diffused, thus shedding light on the behavior of slurry vein propagation.

3.1.1. Evolution of grouting pressure during dual-enhanced stimulation

Fig. 6 displays the variations in grouting pressure for different grouting rates during DES. In Fig. 6, a notable pattern emerged where the grouting pressure rapidly increased and then sharply decreased. Such a trend suggests that the clayey-silty sediments might have undergone splitting, leading to the creation of slurry veins—a characteristic typically observed in the fracturing of hard rock (Gustafson and Stille, 1996; Saeidi et al., 2013). Due to the brittleness and elasticity of hard rock, it can sustain the creation of extended, thin fractures within a single fracturing event. Consequently, the pressure curve showcases a swift escalation followed by a steep decline (Gustafson and Stille, 1996; Saeidi et al., 2013). However, such fracture initiation characteristics was not present in all grouting pressure curves, which might relate to the mechanical properties of clayey-silty sediments. The modeled clayey-silty sediments were characterized by poor cementation, weak elasticity, and high plasticity (Ye et al., 2020). As the slurry infiltrated and compressed the surrounding sediments, there was an increase in pressure. When this pressure surpassed the sediment's failure strength, it caused the sediments to split, enabling the slurry to push forward and resulting in a reduction of pressure (Lan et al., 2020). But at lower grouting rate (Fig. 6(d)), increased slurry filtration made it challenging for grouting pressure to climb swiftly, which may prevent sediments splitting and resulting in compaction rather than splitting grouting. Hence, compaction grouting likely took place during run 9, a scenario that was similarly witnessed in prior experiments involving cement slurry injection (Kleinlugtenbelt, 2005; Bezuijen et al., 2007).

In contrast to hard rock, where hydraulic fracturing occurs relatively easily, the initiation of fractures in soft soil is more demanding, and slurry diffusion within soft soils is typically described as a three-stage process: (1) filling and compaction, where slurry discharged from the grouting outlet compacts and plastically deforms the adjacent soil; (2) splitting, where elevated pressure induces soil shear failure and creates fractures (Zhang et al., 2018); (3) diffusion, where slurry flows into and diffuses through the fractures until the pressure at the fracture tip no longer supports additional soil splitting (Zhang et al., 2020a; Hao et al., 2023). Typically, in soft soils, slurry vein expansion is characterized by a cycle of “diffusion, pause, further diffusion, and another pause” (Cheng et al., 2021). When the pressure at the leading edge of the slurry vein is insufficient to continue fracturing the soil, diffusion comes to a halt causing grouting pressure to rise again. If grouting continues, the increased pressure leads to a rapid widening of the slurry vein. Due to the high porosity of the clay-silty sediment, the filtration loss of the slurry in the reservoir is significant. Additionally, the extrusion of the slurry causes plastic deformation of the sediment, increasing the width of slurry vein. As a result, the grouting pressure rises slowly before the next split occurs, as shown in Fig. 7. Thus, within the pressure curves, we observe multiple instances of sudden pressure drops followed by

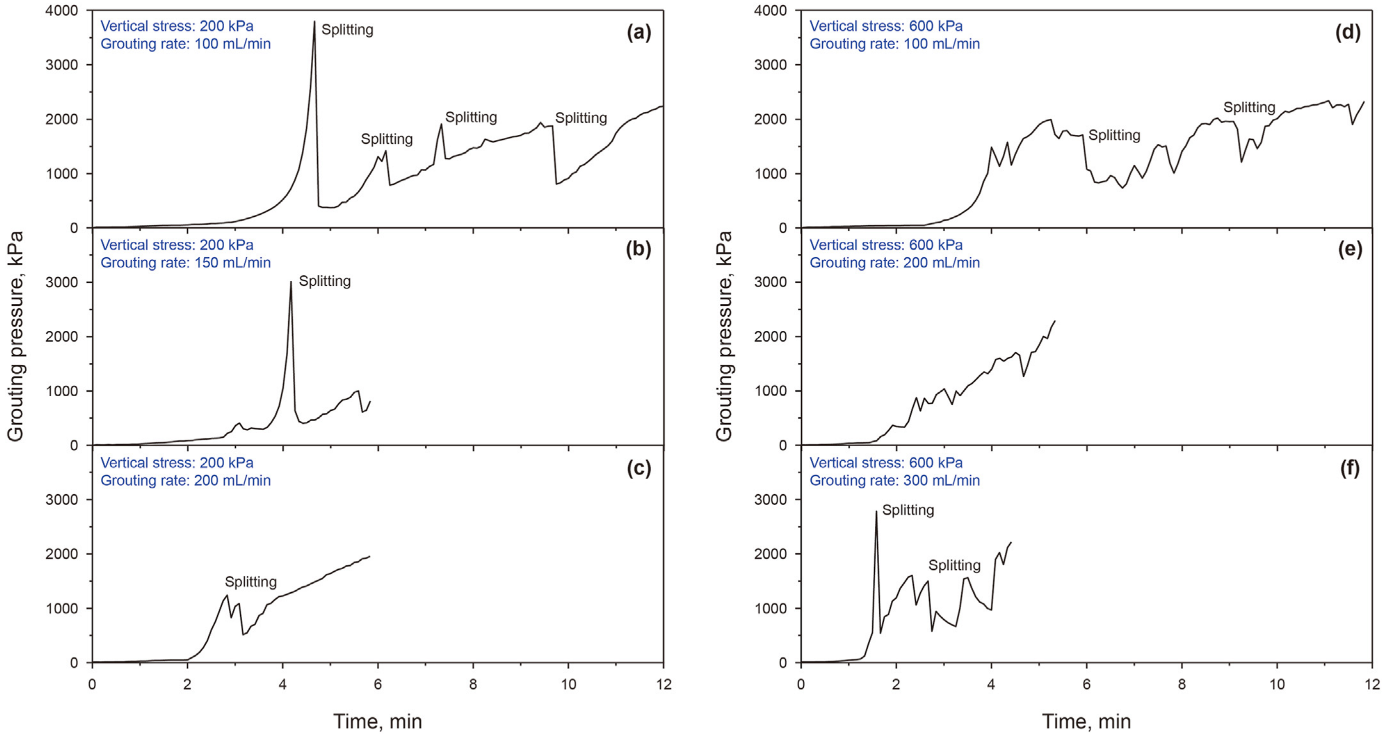

Fig. 6. Evolution of grouting pressure under the condition of different grouting rates.

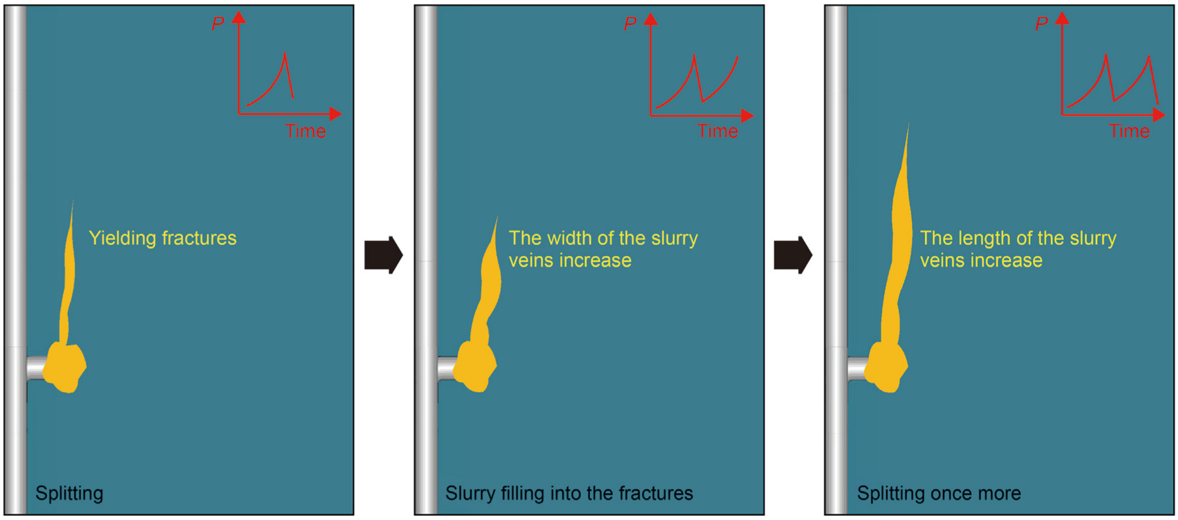

Fig. 7. Schematic diagram of slurry vein formation.

gradual increases. Therefore, the formation of slurry veins is a continuous cycle of "splitting into fractures and filling with slurry".

It is noteworthy that at a vertical stress of 200 kPa, as the grouting rate increased, the number of splitting decreased. This suggests that a higher grouting rate enhanced the fracturing effect in soft clayey-silty sediments, resulting in larger fractures from a single splitting event. The rate at which grout was applied influenced the rapidity of mechanical force transmission to the sediments. At lower rates, this force was imparted more gently to clayey-silty sediments, which initially led to their compaction and resulted in plastic deformation along with enhanced mechanical integrity. Such reinforcement can inhibit the immediate onset of splitting. Fractures only formed when the applied force from the slurry overcame the sediment strength, and due to the constrained energy from fluid refilling, these fractures tended to be smaller with slower propagation of the slurry. As evident in Fig. 6(a) and (b), the initial occurrence of fracture initiation characteristics took a longer time and required greater pressure, suggesting a certain degree of compaction of the sediments around the grouting pipe. Under a vertical stress of 600 kPa, the grouting pressure curve exhibited a significant increase in fluctuation frequency, indicative of multiple splitting and slurry filling events occurring within the sediments. This demonstrates that increased vertical stress heightened the difficulty of slurry vein formation through splitting, with each splitting event yielding smaller fracture sizes and limiting the extent of slurry vein expansion in a single splitting event. With the increase in grouting rate, the frequency of fluctuations in the grouting pressure curve decreased, and a phase of steady rise became apparent. This suggests that the fractures generated by splitting were larger, allowing for greater expansion distances of the slurry veins. This data implies that lower grouting rates made slurry vein formation difficult, whereas higher rates led to a more uniform pressure curve and better vein formation in the soft reservoir.

In the process of split grouting, formation stress is key to starting fractures, guiding slurry diffusion, and forming slurry veins (Yang et al., 2004; Li et al., 2012; Ma et al., 2022). This research also examined how vertical stress affected slurry vein diffusion patterns, with pressure curves shown in Fig. 8. When the grouting rate was 100 mL/min, the frequency of fluctuations in the grouting pressure curve increased with the rise in vertical stress. As mentioned above, at a vertical stress of 200 kPa and a grouting rate of 100 mL/min, a portion of the slurry would compress the sediments adjacent to the grouting pipe prior to the initial splitting, with the remainder generating slender and elongated slurry veins within the sediments. As the vertical stress rose to 600 kPa, the grouting pressure curves exhibited frequent fluctuations, indicating that increased vertical stress led to a higher frequency of smaller fractures and potentially exerted a stronger compressive effect on the sediments surrounding the grouting pipe. At a grouting rate of 200 mL/min with the vertical stress of 200 and 400 kPa, the grouting pressure curves indicated a smooth increase, pointing to the creation of larger fractures and the formation of slender slurry veins within the sediments during each splitting event. However, at a vertical stress of 600 kPa, the pressure curve showed fluctuations, suggesting an increase in sediment compaction activities near the grouting pipe. In essence, with a given grouting rate, a rise in vertical stress impeded slurry vein diffusion, causing more slurry to be used for compaction near the injection point, as evidenced by the post-excavation appearance of the grouting veins.

Fig. 9 depicts the grouting pressure curves for frozen sediments, which were markedly smoother and exhibited fewer fluctuations in pressure during the diffusion stage compared to those of unfrozen sediments. This indicated that initiating fractures in frozen sediments was less challenging, which was conducive to the formation of slender slurry veins. The freezing of water within the pore spaces reinforced the connections between particles and increased the

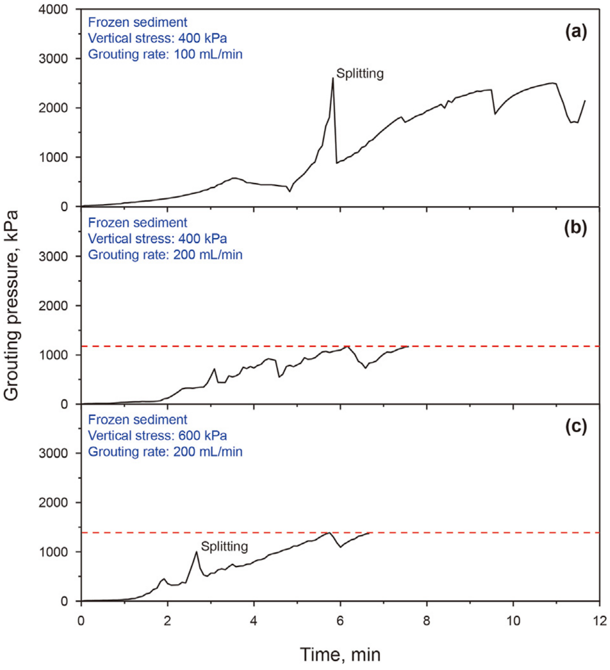

Fig. 9. Evolution of grouting pressure in the frozen sediments.

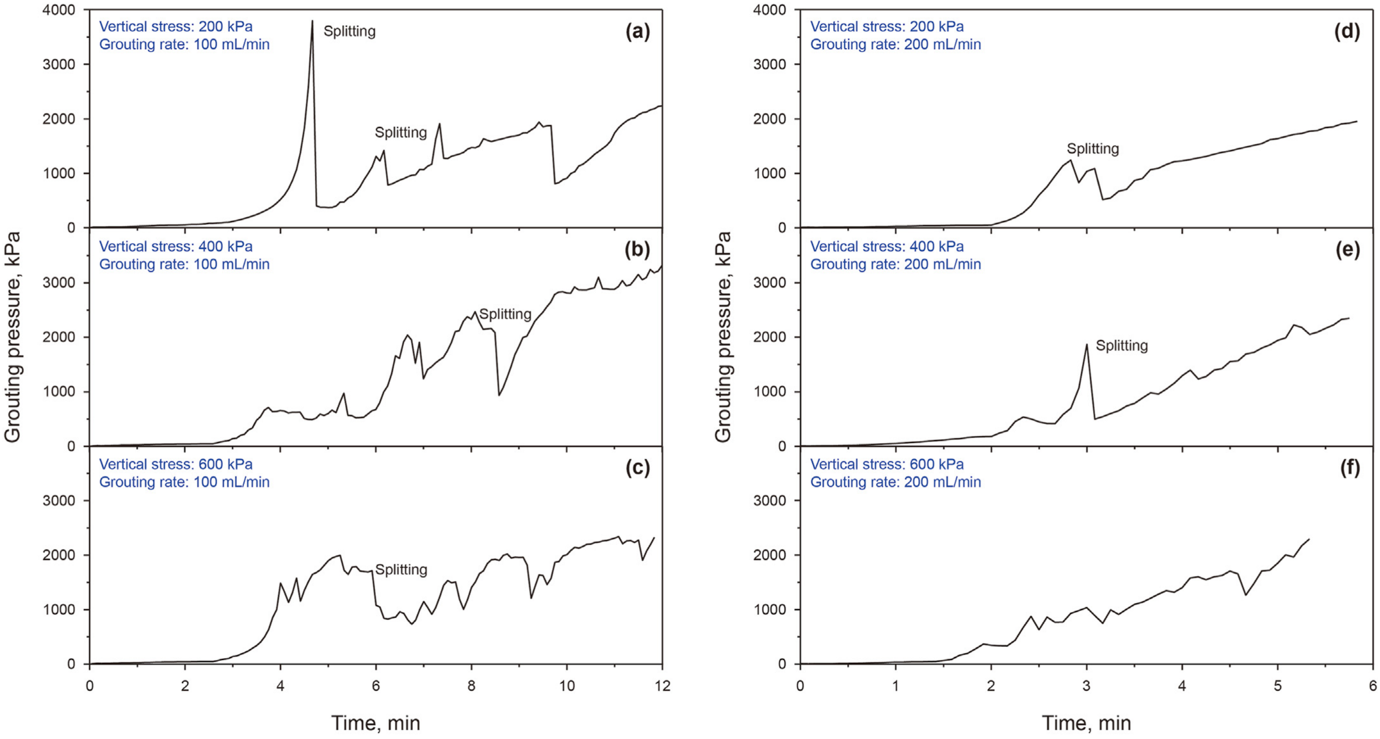

Fig. 8. Evolution of grouting pressure under the condition of different vertical formation stress.

brittleness of the sediment. Consequently, this led to a reduction in soil deformability and energy dissipation, allowing the slurry to be dispersed over larger distances within the reservoir at reduced pressures (Wawersik and Fairhurst, 1970; Zhang et al., 2016). It is notable that in NGH reservoirs, the presence of hydrates in the pores strengthens the interparticle cementation, thereby enhancing the cohesion and modulus of elasticity of the formation (Winters et al., 2007; Lijith et al., 2019; Lu et al., 2022). This phenomenon facilitates the diffusion of the slurry and expanded the reach of reservoir stimulation.

3.1.2. Evolution of formation stress during dual-enhanced stimulation

The diffusion of slurry veins compresses nearby sediments, resulting in elastic-plastic deformation and altering formation stress. These alterations can reveal the diffusion path of the slurry veins. For this study, stress sensors were installed in horizontal and vertical positions to monitor these changes: two sensors were placed laterally along the *x* and *y* axes to observe horizontal stress variations, and one sensor was positioned above the sediment to track vertical stress fluctuations. Fig. 10 illustrates how the formation stress changes in frozen and unfrozen sediments during grouting. The figure suggests an increase in the vertical stress, likely due to the slurry spreading upwards and compressing the sediments. Significantly, there were instances where the vertical stress decreased, signaling those fractures occurred within the sediments. These events transpired as the slurry entered and filled the freshly formed fractures, with the elastic recovery of the sediments leading to a momentary diminution in the vertical stress. Due to the vertical stress exerted on the upper part of the reactor, the vertical axis corresponded to the maximum principal stress and the horizontal axis to the minimum principal stress. This indicates that slurry veins were inclined to extend in alignment with the maximum principal stress direction, consistent with the fracture propagation direction typically observed in the hydraulic fracturing of rock and soil (Zhang et al., 2019b; Ma et al., 2022).

As the slurry fractured the sediments, it formed slurry veins that pushed against the sediment ahead during their advancement, resulting in an increase in horizontal stress. The patterns of stress sensor readings across different locations suggested the directions of slurry vein diffusion in the horizontal plane. The horizontal stress curve, unlike the vertical stress curve, was characterized by a smooth and progressive increment, reflecting the multidirectional radial expansion of the slurry veins. The growth trends in horizontal stress differed depending on the sensor location, which were closely related to their proximity to the expanding slurry veins. At a vertical stress of 200 kPa and a grouting rate of 100 mL/min, a significant increase in horizontal stress was noted on one side, suggesting a predominant diffusion of the slurry vein towards the H2 stress sensor. This pattern was also observed with grouting in frozen sediments under a vertical stress of 400 kPa and a grouting rate of 100 mL/min. When the grouting rate increased to 150 and 200 mL/min, the horizontal stress rose in both directions, indicating that slurry veins were expanding towards both horizontal stress sensors. Notably, during grouting in frozen sediment at a vertical stress of 600 kPa and a grouting rate of 200 mL/min, a horizontal stress sensor reported a sharp increase in the late stages of grouting suggesting that as the slurry reached the reactor's edge, further injection was impeded, leading to slurry pile-up and a sharp rise in stress in that region.

3.2. The morphology of slurry veins and the stimulation area

In the process of DES, the objective is to create an extensive and complex network of slurry veins within the reservoir, allowing for the efficient transport of gas and water (Feng et al., 2019; Sun et al., 2019a; Li et al., 2020). To further investigate the effects of reservoir stress and grouting rate on the morphology of slurry veins, the

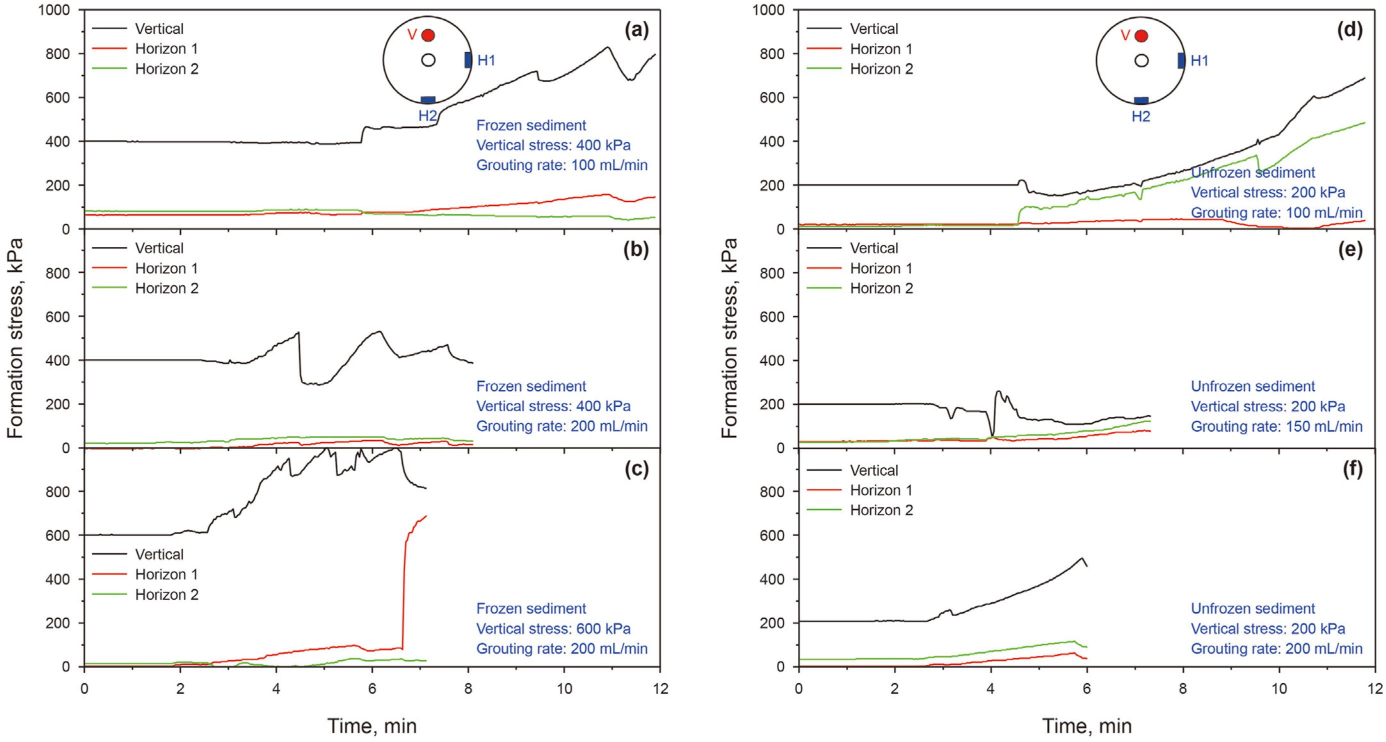

Fig. 10. Evolution of formation stress during the diffusion of slurry veins.

sediments were excavated to obtain the slurry veins and then the tests and measurements were conducted on them. Table 3 gives the detailed measurements of properties of slurry veins.

3.2.1. *Effect of grouting rate on the morphology of slurry veins*

Fig. 11 depicts the influence of grouting rate on the morphology of the slurry veins. The examination of the unearthed slurry veins revealed a consistent pattern in their formation, with a progressive decrease in thickness as the distance from the grouting source increased. This trend suggests that as the slurry traveled through the fractures during the grouting process, energy was dissipated, resulting in a continuous tapering of the slurry veins' width with extension (Yun et al., 2007). Reportedly, at low grouting rates, the slurry vein had a small diffusion distance and formed a large consolidation body around the grouting pipe (Hao et al., 2023), while higher grouting rates resulted in increased diffusion distance and the formation of additional branching veins (Ma et al., 2021). Our study similarly observed this phenomenon. Under a vertical stress condition of 200 kPa, an increase in the grouting rate resulted in the slurry veins exhibiting a more complex morphology and diffusion direction. It is noteworthy that the diffusion direction of the slurry veins aligns with the stress variations illustrated in Fig. 10. At a vertical stress of 400 kPa, the diffusion distance of the slurry vein was 140 mm at a grouting rate of 200 mL/min, which was notably greater than the 109 mm observed at 100 mL/min. Surprisingly, under a vertical stress of 600 kPa and a grouting rate of 100 mL/min, no slurry veins were present. Instead, compaction grouting took place in the sediments, forming a consolidated body near the grouting pipe. This indicates that the slurry effectively compacted the sediments without causing splitting or the formation of slurry veins, as seen in the grouting pressure curve pattern (Fig. 6). An increase in the grouting rate to 200 mL/min resulted in the appearance of a single wing vein in the sediments, while further increasing the rate to 300 mL/min led to the formation of double wing slurry veins. The results show that at lower grouting rates, the slurry mainly accumulated near the grouting pipe. However, as the grouting rate increased, the slurry spread further, leading to a more intricate pattern of slurry veins. In summary, the initial injection of grout resulted in elastic-plastic deformation in the sediments, storing energy as plastic strain (Li et al., 2014). Subsequent injections increased grouting pressure, compacted the soil, and created stress concentration until the reservoir eventually failed. Higher grouting rates elevated sediment strain rates (Ma et al., 2022), increasing the likelihood of reservoir splitting, while also extending the diffusion distance of the slurry.

3.2.2. *Effect of vertical stress on the morphology of slurry veins*

It is widely known that hydraulic fracturing fissures and grout veins propagate along the direction of maximum principal stress (Zhang et al. 2019b, 2020a; Ma et al., 2022). As shown in Fig. 12, as the vertical stress increased from 0 to 600 kPa, the direction of slurry vein diffusion shifted from horizontal to vertical. This indicates that the diffusion of slurry veins followed the direction of the maximum principal stress. In the absence of vertical stress, the slurry diffused horizontally to form uniform 1 mm thick slurry veins with a 150 mm diffusion radius. However, with the application of vertical stress, the slurry diffused vertically, leading to consolidation around the grouting pipe. This resulted in significant thickness variations between veins at different distances. At 200 kPa of vertical stress, the slurry veins followed a regular shape, while at 400 kPa, the veins deflected during the diffusion process. Interestingly, at 600 kPa of vertical stress, the slurry only accumulated around the grouting port without forming distinct veins. This observation suggests that increasing vertical stress does not necessarily promote slurry vein diffusion. This conclusion is supported by consistent results from two grouting tests conducted to minimize test variability. During the diffusion of the slurry veins, they encountered resistance from the sediments (Zhu et al., 2021). As the diffusion distance of the slurry increased, the resistance it needed to overcome also increased, leading to a weakening of the energy transmission effect, which resulted in increased pressure at the injection port and decreased pressure at the leading edge of the slurry vein (Li et al., 2021b). Consequently, the energy to split the sediments decreased, which led to a reduction in the thickness of the slurry vein's front end and an increase in the randomness of its diffusion direction (Li et al., 2018b). At an injection rate of 200 mL/min, higher vertical stress led to simpler slurry vein morphologies. Specifically, at 200 kPa, one large vertical vein and one small horizontal vein formed; at 400 kPa, one large vertical vein and one small vertical vein formed; and at 600 kPa, only one large vertical vein was observed. The results indicate that high reservoir stress hindered the formation of complex slurry veins at the same grouting rate. Increasing the grouting rate was found to be an effective way to achieve longer diffusion distances and more complex veins in the reservoir under high-stress conditions.

Table 3
The properties of slurry veins.

Run	Grouting parameters			Properties of slurry veins			
	Vertical stress, kPa	Grouting rate, mL/min	Frozen sediment	Diffusing distance, mm	Thickness, mm	Surface area, cm^2	Number of slurry veins
1	0	100	NO	150	1–2	/	1
2-1	200	100	NO	125	2–4	/	3
2-2	200	100	NO	132	1–3	652.0	3
3	200	150	NO	140	1–3	/	1
4-1	200	200	NO	145	1–4	/	2
4-2	200	200	NO	142	2–4	682	2
5-1	400	100	NO	112	1–3	/	2
5-2	400	100	NO	109	2–5	591	2
6	400	100	YES	122	2–4	/	2
7-1	400	200	NO	140	1–3	/	2
7-2	400	200	NO	123	1–3	642	2
8	400	200	YES	110	1–4	/	2
9-1	600	100	NO	Compaction grouting, no slurry veins			
9-2	600	100	NO	Compaction grouting, no slurry veins			
10	600	200	NO	150	2–4	539	1
11	600	200	YES	150	1–3	/	3
12	600	300	NO	130	2–4	572	2

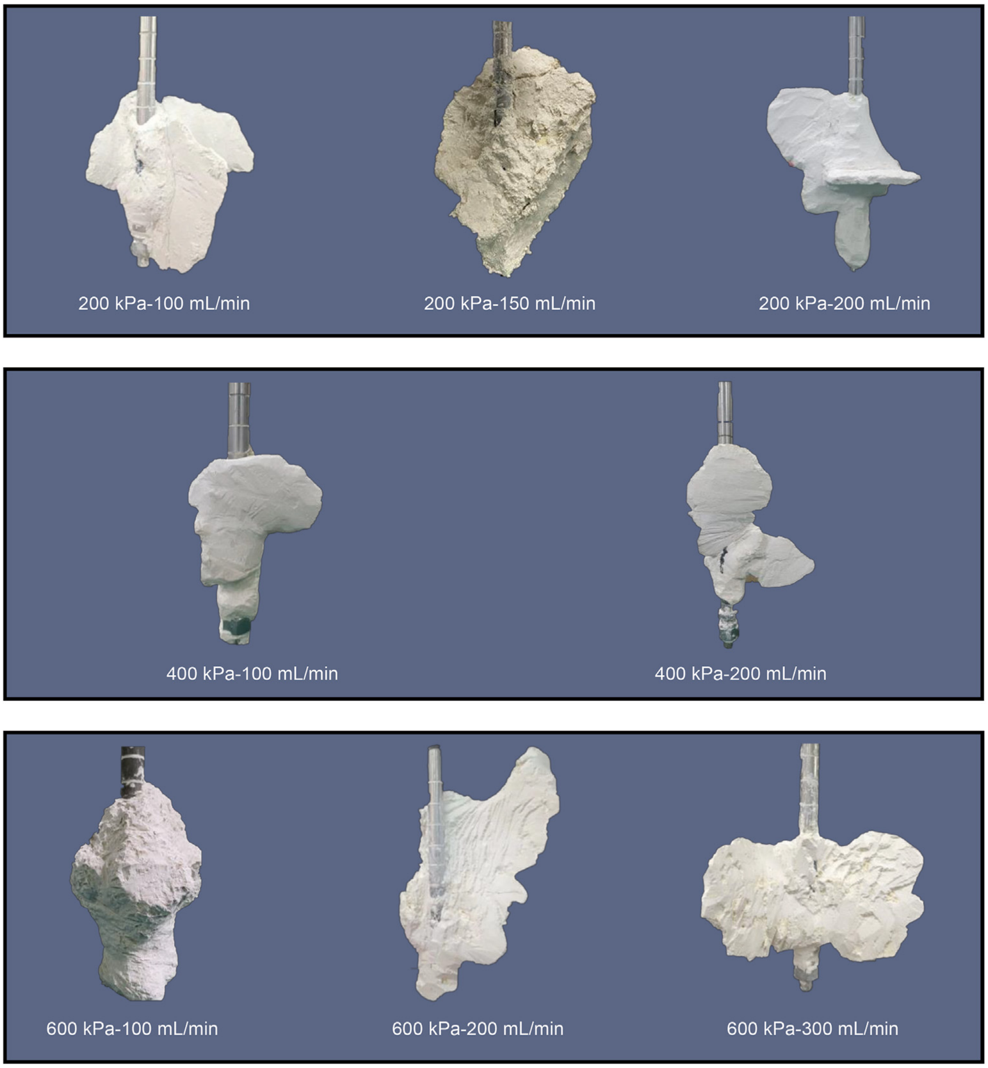

Fig. 11. The morphology of slurry veins under the condition of different grouting rates.

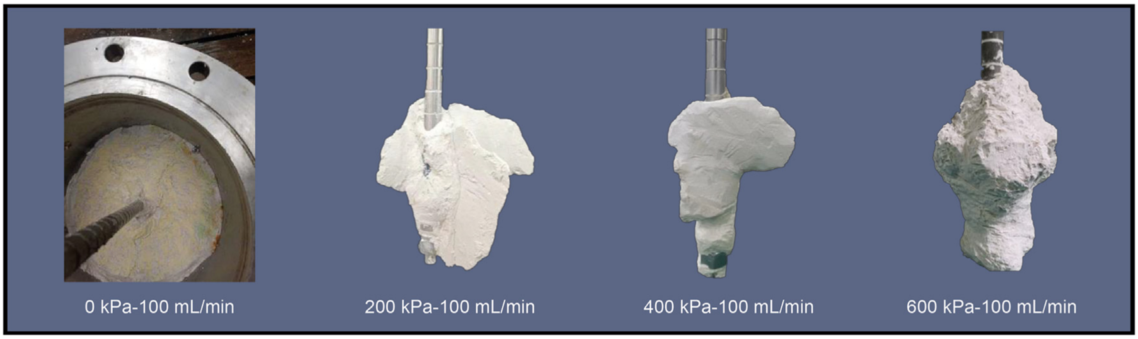

Fig. 12. The morphology of slurry veins under the condition of different vertical stress.

3.2.3. *Effect of elastic modulus of sediments on the morphology of slurry veins*

Typically, increasing soil cohesion enhances the adhesion between soil particles, thereby increasing soil deformation resistance and elastic modulus, resulting in harder and less prone to plastic deformation soil (Luo et al., 2020; Lu et al., 2022). In addition, the increased cohesion within sediments enhanced their brittleness, which was beneficial for the initiation and propagation of artificial fractures (Yang et al., 2020). In this study, freezing the sediment resulted in ice within the pores, enhancing the cementation strength between the particles. Triaxial compressive strength tests indicated an increase in both cohesion and internal friction angle (Fig. 5), signifying heightened sediment elastic modulus and brittleness. In the case of frozen sediments, the formation of slurry veins exhibited a relatively straight trend with greater longitudinal height, indicating a more stable diffusion of slurry within the sediments after splitting (Fig. 13). Similarly, long, flat penetrating fractures have been observed in hydraulic fracturing tests involving other frozen sediments and hydrate sediments (Max, 2003; Yang et al., 2020). These findings highlight that the enhanced elastic modulus and brittleness of the reservoir facilitate the diffusion of fractures or veins, leading to the formation of veins with a larger diffusion radius and a more regular shape. Fortunately, in the case of NGH reservoirs, the presence of hydrates in the pores serves to enhance the cementation between sediment particles, similar to frozen pore water (Yun et al., 2007; Luo et al., 2016; Lu et al., 2022). This augmentation results in an improved elastic modulus and brittleness of the reservoir, which is beneficial for the diffusion of slurry within hydrate reservoirs and the formation of a complex slurry veins network (Yang et al., 2020).

3.2.4. *Effective stimulation area*

The area of pressure relief serves as an important measure for assessing the success of reservoir stimulation (Aghajari et al., 2019; Feng et al., 2019; Sun et al., 2019a; Zhang et al., 2019a; Li et al., 2020). In this study, the surface area of the slurry veins, which we analyzed to ascertain the pressure relief area post-DES, was meticulously quantified through three-dimensional laser scanning. This quantified surface has been termed the “effective stimulation area”.

Fig. 14 depicts the three-dimensional morphology of slurry veins and includes measurements of their length, width, and height. Table 3 provides the calculated surface area of slurry veins and the effective stimulation area. Fig. 15 illustrates the relationship between the effective stimulation area of the reservoir and the variation in grouting rate and vertical stress. The surface area of the slurry vein increased with higher grouting rates, although the increment was relatively modest when the grouting rate was raised by 100 mL/min. Specifically, under vertical stress of 200, 400, and 600 kPa, a 100 mL/min increase in grouting rate resulted in a 4.6%, 8.6%, and 6.1% increase in the surface area of the slurry veins, respectively. The limited increase in surface area with higher grouting rates can be attributed to the small scale of the reactor, causing the slurry veins to extend to the outer edge of the reactor. In contrast, as the vertical stress increased with a constant grouting rate, there was a gradual decrease in the surface area of the slurry vein. Particularly noteworthy was the significant reduction in the surface area of the slurry veins when the vertical stress reached 600 kPa, as illustrated in Fig. 15. This indicates the difficulty in the diffusion of the slurry veins in soft sediments under increased vertical stress. Therefore, in practical DES processes, where reservoir stress remains constant and there is a possibility of increased stress during grouting, higher grouting rates should be utilized to maximize the stimulation area.

3.3. *The porosity and pore structure of slurry veins*

To evaluate the permeability improvement from DES, we measured the porosity and pore structure of slurry veins using mercury intrusion porosimetry. In runs 7-1 and 12-1, small cubic samples near, halfway, and far from the grouting pipe (refer to Fig. 16) were tested.

Fig. 17 presents the relationship between mercury injection volumes and pore sizes in slurry veins, showing a similar pore size distribution for samples taken near, halfway, and far from the grouting pipe under varying grouting conditions. This uniformity in pore sizes suggests that the diffusion of the slurry veins didn't have a noticeable effect on their porosity, pointing to an even distribution during the diffusion. Table 4 details the range of pore sizes observed in the slurry veins. There was little variation in effective porosity among the different locations, with values ranging from 65% to 70%, which is essentially the same as that of the slurry consolidated body made in the laboratory (68%) (Sun et al., 2022). Likewise, the median pore sizes were quite consistent, lying between 11 and 15 μm. The largest pores identified were around 800 μm, and the smallest were near 5.48 μm, which is essentially larger than that of the slurry consolidated body made in the laboratory (400 μm). The pore size distribution for each sample peaked sharply, with the predominant pore size being about 11 μm, which made up over 15% of the total pore volume. These results indicate that the cured slurry veins created a porous network with good connectivity, mainly comprising smaller pores, which helps improve permeability and sand control. However, it should be noted that the proportion of “large pores”, those with a radius greater than 100 μm, varied (as highlighted in Fig. 17). Samples taken closer to the grouting pipe contained a greater fraction of these large pores, and this fraction diminished with distance from the pipe. This pattern was attributed to the higher initial pressure near the pipe, which resulted in a tighter packing of the pore-forming agents. As the slurry moved away and the pressure decreased, the packing of these agents became less dense, resulting in a reduction of large pores in the areas farther from the pipe.

4. Conclusions

This paper introduced the DES method for marine hydrate reservoirs and presented experimental studies of split grouting with dual-enhanced slurry into clayey-silty reservoirs to assess its viability. The study focused on the diffusion characteristics of the slurry and the morphology of the veins within these sediments. Furthermore, it assessed the effective stimulation area of the reservoir and analyzed the pore size and porosity of the veins. The

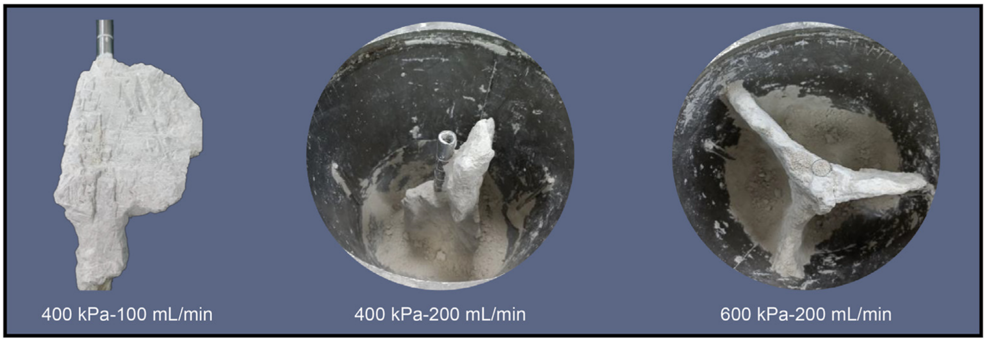

Fig. 13. The morphology of slurry veins within frozen sediments.

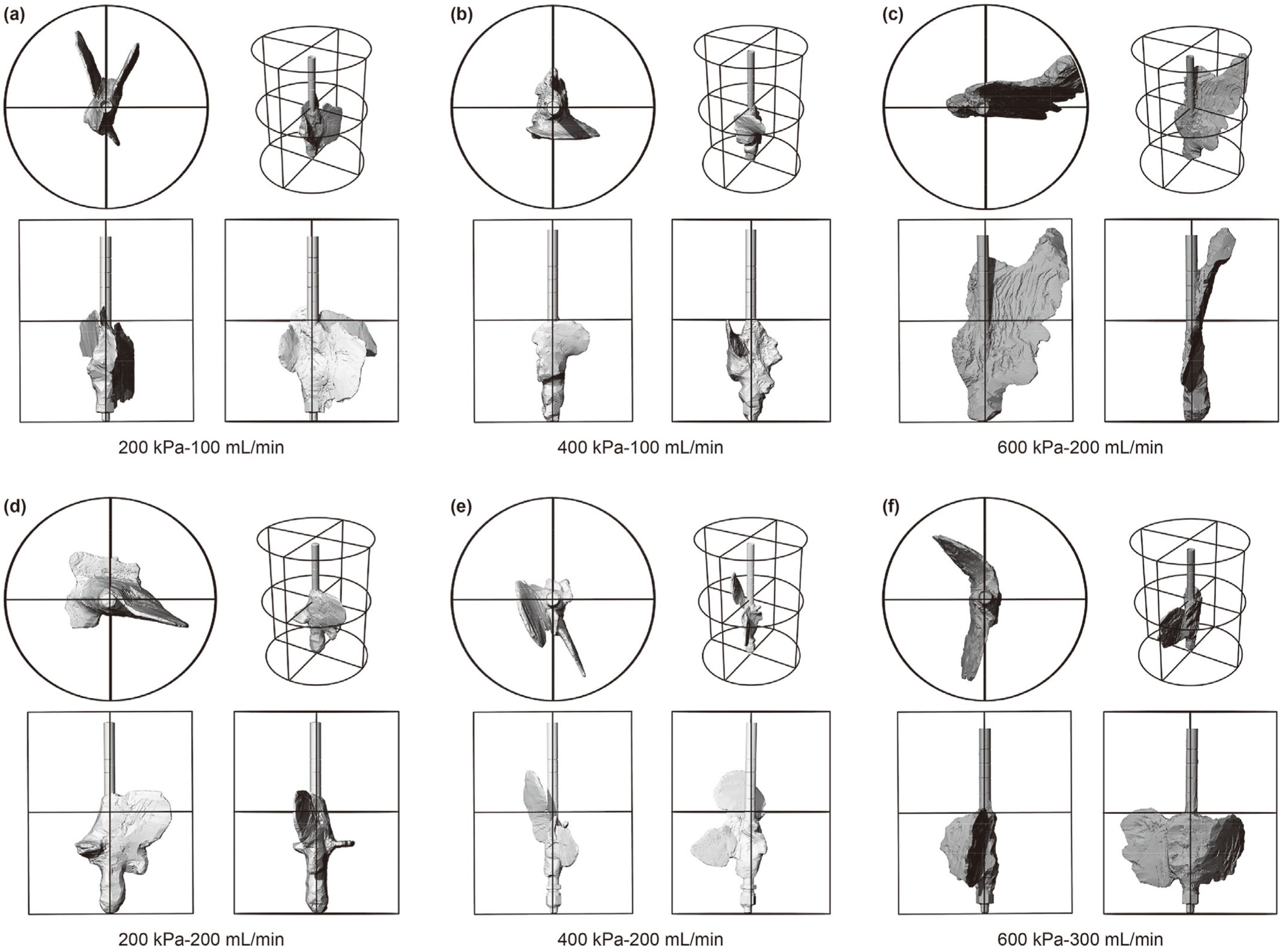

Fig. 14. The three-dimensional morphology of slurry veins.

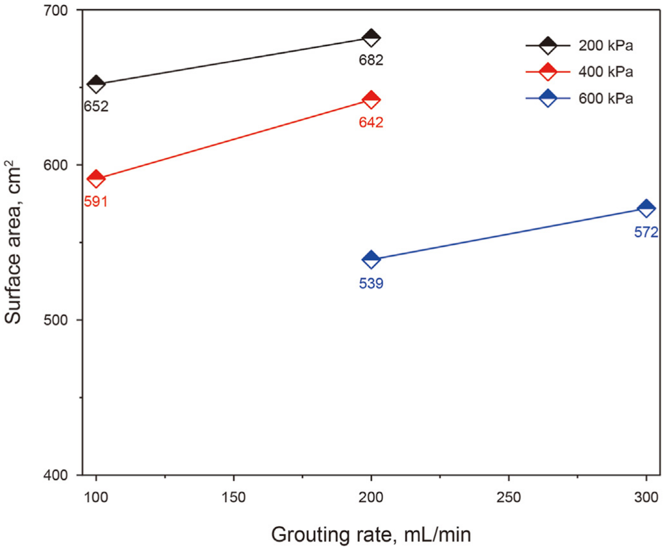

Fig. 15. The surface area of slurry vein.

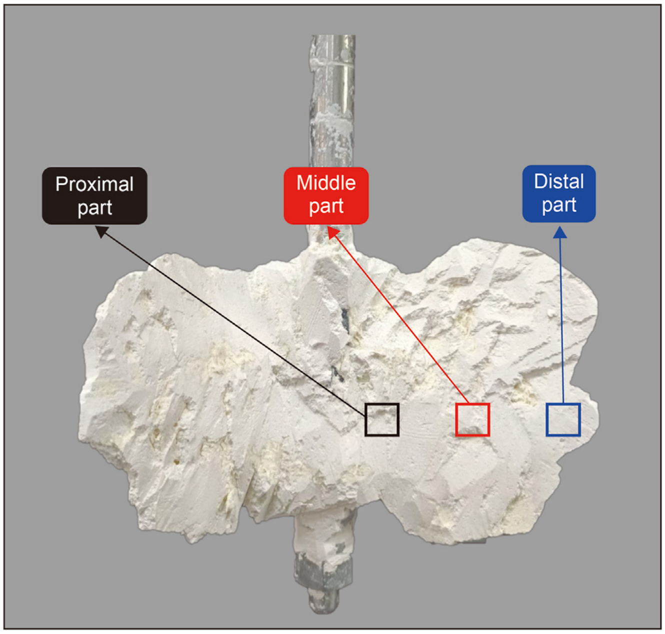

Fig. 16. Sample location for mercury intrusion porosimetry tests.

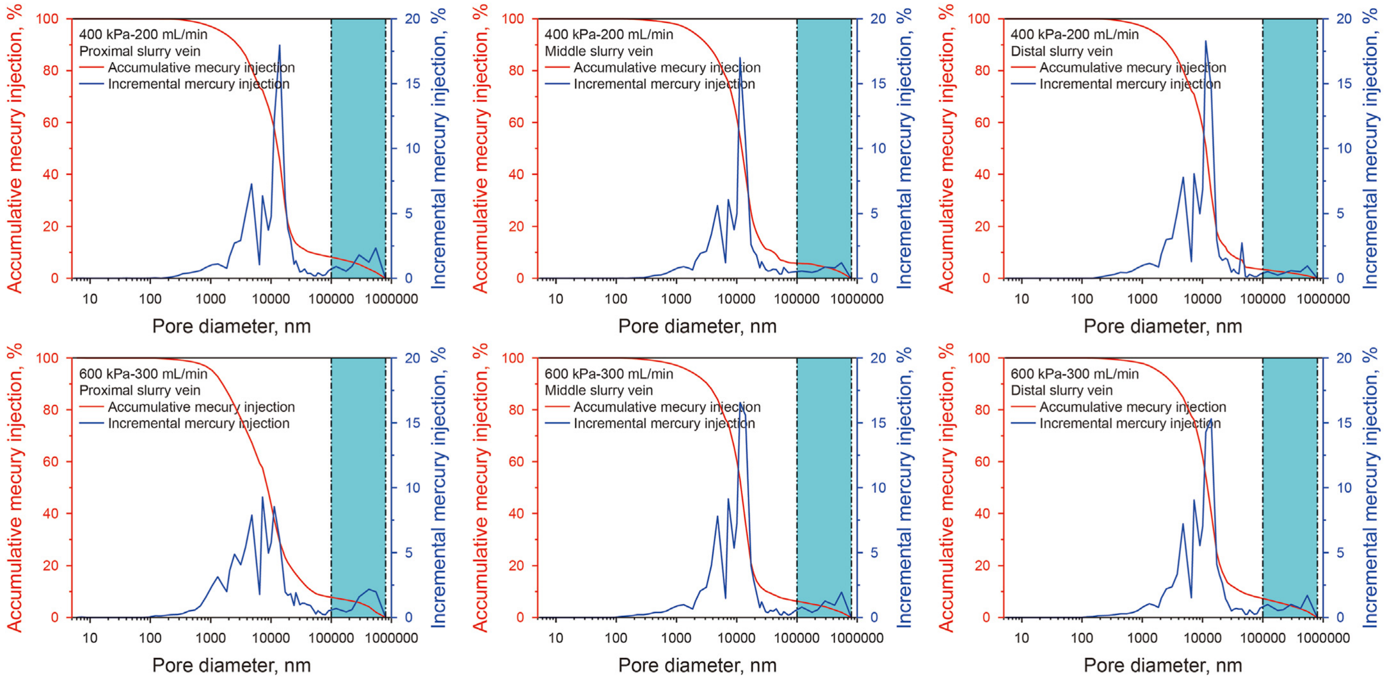

Fig. 17. Accumulative and incremental mercury injection versus pore size curve of slurry veins.

Table 4
Pore structure and porosity of the slurry veins.

Run	Porosity, %			Maximum pore, μm			Median pore, μm			Minimum pore, μm		
	Proximal	Middle	Distal	Proximal	Middle	Distal	Proximal	Middle	Distal	Proximal	Middle	Distal
Run 7-1	66.77	69.43	66.38	795.06	787.54	795.91	13.09	14.84	11.46	5.48	5.48	5.48
Run 12-1	65.06	65.67	67.69	799.77	793.92	798.57	8.75	11.80	12.13	6.03	5.48	5.48

main findings of this study are as follows.

(1) Similar to hydraulic fracturing, the process of split grouting with dual-enhanced slurry also exhibited fracture initiation characteristics, where the pressure curve demonstrated a rapid escalation followed by a sharp decline. However, there were typically more instances of fracture initiation and the magnitude of pressure fluctuations was smaller, indicating that the fractures created in clayey-silty sediments were relatively short. Additionally, the diffusion of slurry veins followed the direction of the maximum principal stress. As vertical stress increased, the orientation of the slurry veins shifted from horizontal to vertical.

(2) In contrast to hydraulic fracturing in hard rocks, the process of split grouting with dual-enhanced slurry within clayey-silty sediments encountered more demanding conditions for the formation of slurry veins, easily leading to compaction grouting. The formation of these veins was marked by a repetitive cycle of “splitting into fractures and then filling with slurry.” The weaker the sediment, the slower the rate of injection, and the higher the vertical stress, the more often these cycles occurred.

(3) The slurry veins that were formed within the sediments through split grouting techniques were continuous and stable, with their thickness diminishing as the diffusion distance increased. The morphology of these veins was influenced by factors such as the grouting rate, formation stress, and elastic modulus. Higher grouting rates and elastic moduli facilitated the diffusion of the slurry and the formation of complex vein networks. Conversely, increased reservoir stress impeded the formation and diffusion of these veins, often resulting in compaction grouting.

(4) To assess the permeability increasing provided by the DES method, mercury intrusion porosimetry was employed to evaluate the porosity and pore structure of the slurry veins. The effective porosity across various locations—near, mid-distance, and far from the grouting pipe—showed minimal variation, consistently ranging from 65% to 70%. Similarly, median pore sizes remained relatively stable, between 11 and 15 μm. These findings suggest that the solidified slurry veins form a well-connected porous network predominantly composed of smaller pores, enhancing both permeability and sand control capabilities.

CRediT authorship contribution statement

Yun Qi: Writing – original draft, Methodology, Investigation, Formal analysis, Data curation. **You-Hong Sun:** Supervision, Project administration, Funding acquisition, Conceptualization. **Bing Li:** Writing – review & editing, Methodology, Investigation, Formal analysis. **Heng-Feng Shan:** Investigation, Data curation. **Yi-Zhuo Liu:** Investigation. **Guo-Biao Zhang:** Writing – review & editing, Writing – original draft, Methodology, Investigation, Formal analysis, Conceptualization.

Declaration of competing interest

The authors declare that they have no known competing financial interests or personal relationships that could have appeared to influence the work reported in this paper.

Acknowledgments

The financial support received from the National Natural Science Foundation of China (Nos. 51991364, and 42202347).

References

Aghajari, H., Moghaddam, M.H., Zallaghi, M., 2019. Study of effective parameters for enhancement of methane gas production from natural gas hydrate reservoirs. Green Energy Environ. 4 (4), 453–469. https://doi.org/10.1016/j.gee.2018.04.002.

Bezuijen, A., Sanders, M., Hamer, D., et al., 2007. Laboratory tests on compensation grouting, the influence of grout bleeding. 33rd ITA-AITES World Tunnel Congress.

Boswell, R., Collett, T.S., 2011. Current perspectives on gas hydrate resources. Energy Environ. Sci. 4 (4), 1206–1215.

Chen, C., Yang, L., Jia, R., et al., 2017. Simulation study on the effect of fracturing technology on the production efficiency of natural gas hydrate. Energies 10 (8), 16. https://doi.org/10.3390/en10081241.

Chen, M., Li, Y., Zhang, Y., et al., 2023. Recent advances in creep behaviors characterization for hydrate-bearing sediment. Renew. Sustain. Energy Rev. 183, 113434. https://doi.org/10.1016/j.rser.2023.113434.

Cheng, S., Yang, F., Dai, Y., et al., 2021. An experimental research on crack propagation regularity during fracture grouting. IOP Conference Series: Earth and Environmental Science. IOP Publishing, 032047. https://doi.org/10.1088/1755-1315/651/3/032047.

Collett, T.S., 2002. Energy resource potential of natural gas hydrates. AAPG Bull. 86 (11), 1971–1992. https://doi.org/10.1306/61EEDDD2-173E-11D7-8645000102C1865D.

Draganović, A., Stille, H., 2011. Filtration and penetrability of cement-based grout: study performed with a short slot. Tunn. Undergr. Space Technol. 26 (4), 548–559. https://doi.org/10.1016/j.tust.2011.02.007.

Feng, Y., Chen, L., Suzuki, A., et al., 2019. Enhancement of gas production from methane hydrate reservoirs by the combination of hydraulic fracturing and depressurization method. Energy Convers. Manag. 184, 194–204. https://doi.org/10.1016/j.enconman.2019.01.050.

Fink, J., 2021. Petroleum Engineer's Guide to Oil Field Chemicals and Fluids. Gulf Professional Publishing.

Guo, C., Sun, B., Hu, D., et al., 2019. A field experimental study on the diffusion behavior of expanding polymer grouting material in soil. Soil Mech. Found. Eng. 56 (3), 171–177. https://doi.org/10.1007/s11204-019-09586-7.

Gustafson, G., Stille, H., 1996. Prediction of groutability from grout properties and hydrogeological data. Tunn. Undergr. Space Technol. 11 (3), 325–332. https://doi.org/10.1016/0886-7798(96)00027-2.

Hao, Y., Guo, C., Shi, M., et al., 2023. Application of polymer split grouting technology in earthen dam: diffusion law and applicability. Construct. Build. Mater. 369, 130612. https://doi.org/10.1016/j.conbuildmat.2023.130612.

Hayashi, K., Haimson, B.C., 2012. Characteristics of shut-in curves in hydraulic fracturing stress measurements and determination of in situ minimum compressive stress. J. Geophys. Res. Solid Earth 96 (B11), 18311–18321. https://doi.org/10.1029/91jb01867.

Kleinlugtenbelt, R., 2005. Compensation Grouting: Laboratory Experiments in Sand.

Konno, Y., Jin, Y., Yoneda, J., et al., 2016. Hydraulic fracturing in methane-hydrate-bearing sand. RSC Adv. 6 (77), 73148–73155. https://doi.org/10.1039/C6RA15520K.

Lan, X., Zhang, X., Li, X., et al., 2020. Experimental study on grouting reinforcement mechanism of heterogeneous fractured rock and soil mass. Geotech. Geol. Eng. 38 (5), 4949–4967. https://doi.org/10.1007/s10706-020-01338-x.

Li, B., Ma, X., Zhang, G., et al., 2020. Enhancement of gas production from natural gas hydrate reservoir by reservoir stimulation with the stratification split grouting foam mortar method. J. Nat. Gas Sci. Eng. 81, 103473. https://doi.org/10.1016/j.jngse.2020.103473.

Li, J., Ye, J., Qin, X., et al., 2018a. The first offshore natural gas hydrate production test in South China Sea. China Geology 1 (1), 5–16. https://doi.org/10.31035/cg2018003.

Li, L.C., Tang, C.A., Li, G., et al., 2012. Numerical simulation of 3D hydraulic fracturing based on an improved flow-stress-damage model and a parallel FEM technique. Rock Mech. Rock Eng. https://doi.org/10.1007/s00603-012-0252-z.

Li, P., Zhang, Q., Zhang, X., et al., 2014. Analysis of fracture grouting mechanism based on model test. Rock Soil Mech. 35 (11), 3221–3230 (in Chinese).

Li, S., Wu, D., Wang, X., Hao, Y., 2021a. Enhanced gas production from marine hydrate reservoirs by hydraulic fracturing assisted with sealing burdens. Energy 232, 120889. https://doi.org/10.1016/j.energy.2021.120889.

Li, X., Hao, M., Zhong, Y., et al., 2021b. Experimental study on the diffusion characteristics of polyurethane grout in a fracture. Construct. Build. Mater. 273, 121711. https://doi.org/10.1016/j.conbuildmat.2020.121711.

Li, Y., Wu, D., Wu, P., et al., 2021c. Mechanical characteristics of the hydrate-bearing sediments in the South China Sea using a multistage triaxial loading test. Energy Fuels 35 (5), 4127–4137. https://doi.org/10.1021/acs.energyfuels.1c00118.

Li, Y., Hu, Q., Wu, N., et al., 2023. Acoustic characterization for creep behaviors of marine sandy hydrate-bearing sediment. Sci. Rep. 13 (1), 22199. https://doi.org/10.1038/s41598-023-49523-1.

Li, Z., Li, S., Liu, H., et al., 2018b. Experimental study on the reinforcement mechanism of segmented split grouting in a soft filling medium. Processes 6 (8), 131. https://doi.org/10.3390/pr6080131.

Lijith, K., Malagar, B.R., Singh, D.N., 2019. A comprehensive review on the geomechanical properties of gas hydrate bearing sediments. Mar. Petrol. Geol. 104, 270–285. https://doi.org/10.1016/j.marpetgeo.2019.03.024.

Liu, Y., Li, G., Chen, J., et al., 2023. Numerical simulation of hydraulic fracturing-assisted depressurization development in hydrate bearing layers based on discrete fracture models. Energy 263, 126146. https://doi.org/10.1016/j.energy.2022.126146.

Lu, C., Xie, P., Li, H., et al., 2022. Study on the mechanical properties of silty clay sediments with nodular hydrate occurrence. J. Mar. Sci. Eng. 10 (8), 1059. https://doi.org/10.3390/jmse10081059.

Luo, T., Song, Y., Zhu, Y., et al., 2016. Triaxial experiments on the mechanical properties of hydrate-bearing marine sediments of South China Sea. Mar. Petrol. Geol. 77, 507–514. https://doi.org/10.1016/j.marpetgeo.2016.06.019.

Luo, T., Li, Y., Madhusudhan, B., et al., 2020. Comparative analysis of the consolidation and shear behaviors of CH_4 and CO_2 hydrate-bearing silty sediments. J. Nat. Gas Sci. Eng. 75, 103157. https://doi.org/10.1016/j.jngse.2020.103157Getrightsandcontent.

Ma, X., Cheng, J., Sun, Y., Li, S., 2021. 2D numerical simulation of hydraulic fracturing in hydrate-bearing sediments based on the cohesive element. Energy Fuels 35 (5), 3825–3840. https://doi.org/10.1021/acs.energyfuels.0c03895.

Ma, X., Jiang, D., Sun, Y., et al., 2022. Experimental study on hydraulic fracturing behavior of frozen clayey silt and hydrate-bearing clayey silt. Fuel 322, 124366. https://doi.org/10.1016/j.fuel.2022.124366.

Max, M.D., 2003. Natural Gas Hydrate in Oceanic and Permafrost Environments. Springer Science & Business Media.

Moridis, G., Collett, T., 2003. Strategies for gas production from hydrate accumulations under various geologic conditions.

Niu, J., Li, Z., Gu, W., et al., 2020. Experimental study of split grouting reinforcement mechanism in filling medium and effect evaluation. Sensors 20 (11), 3088. https://doi.org/10.3390/s20113088.

Saeidi, O., Stille, H., Torabi, S.R., 2013. Numerical and analytical analyses of the effects of different joint and grout properties on the rock mass groutability. Tunn. Undergr. Space Technol. 38, 11–25. https://doi.org/10.1016/j.tust.2013.05.005.

Sloan Jr, E.D., Koh, C.A., 2007. Clathrate Hydrates of Natural Gases. CRC Press.

Sun, J., Ning, F., Liu, T., et al., 2019a. Gas production from a silty hydrate reservoir in the South China Sea using hydraulic fracturing: a numerical simulation. Energy Sci. Eng. 7 (4), 1106–1122. https://doi.org/10.1002/ese3.353.

Sun, Y., Ma, X., Guo, W., et al., 2019b. Numerical simulation of the short-and long-term production behavior of the first offshore gas hydrate production test in the South China Sea. J. Petrol. Sci. Eng. 181, 106196. https://doi.org/10.1016/j.petrol.2019.106196.

Sun, Y., Shen, Y., Zhang, G., et al., 2022. Performance of dual-increasing stimulation slurry and its consolidating body for submarine hydrate reservoir. Journal of China University of Petroleum (Edition of Natural Science) 46 (6), 1–10 (in Chinese).

Too, J.L., Cheng, A., Khoo, B.C., et al., 2018. Hydraulic fracturing in a penny-shaped crack. Part II: testing the frackability of methane hydrate-bearing sand. J. Nat. Gas Sci. Eng. 52, 619–628. https://doi.org/10.1016/j.jngse.2018.01.046.

Wang, F., Chu, X., Guo, C., 2018a. The feasibility of non-water reaction polymer grouting technology application in seepage prevention for tailings reservoirs. Water Supply 18 (1), 203–213. https://doi.org/10.2166/ws.2017.096.

Wang, X., Sun, Y., Chen, H., et al., 2023. Experimental study on the depressurization of methane hydrate in the clayey silt sediments via hydraulic fracturing. Energy Fuels 37 (6), 4377–4390. https://doi.org/10.1021/acs.energyfuels.2c04282.

Wang, Z., Liao, Y., Zhang, W., et al., 2018b. Coupled temperature field model of gas-hydrate formation for thermal fluid fracturing. Appl. Therm. Eng. 133, 160–169. https://doi.org/10.1016/j.applthermaleng.2018.01.039.

Wawersik, W., Fairhurst, C., 1970. A study of brittle rock fracture in laboratory compression experiments. Int. J. Rock Mech. Min. Sci. Geomech. Abstracts 561–575. https://doi.org/10.1016/0148-9062(70)90007-0.

Winters, W.J., Waite, W.F., Mason, D., et al., 2007. Methane gas hydrate effect on sediment acoustic and strength properties. J. Petrol. Sci. Eng. 56 (1–3), 127–135. https://doi.org/10.1016/j.petrol.2006.02.003.

Yang, L., Shi, F., Yang, J., 2020. Experimental studies on hydraulic fracturing in hydrate sediment. Chem. Technol. Fuels Oils 56 (1), 107–114. https://doi.org/10.1007/s10553-020-01116-8.

Yang, T.H., Tham, L.G., Tang, C.A., et al., 2004. Influence of heterogeneity of mechanical properties on hydraulic fracturing in permeable rocks. Rock Mech. Rock Eng. 37 (4), 251–275. https://doi.org/10.1007/s00603-003-0022-z.

Ye, J., Qin, X., Xie, W., et al., 2020. The second natural gas hydrate production test in the South China Sea. China Geology 3 (2), 197–209. https://doi.org/10.31035/cg2020043.

You, K., Flemings, P.B., Malinverno, A., et al., 2019. Mechanisms of methane hydrate formation in geological systems. Rev. Geophys. 57 (4), 1146–1196. https://doi.org/10.1029/2018RG000638.

Yun, T.S., Santamarina, J.C., Ruppel, C., 2007. Mechanical properties of sand, silt, and clay containing tetrahydrofuran hydrate. J. Geophys. Res. Solid Earth 112 (B4). https://doi.org/10.1029/2006JB004484.

Zhang, C., Yue, W., Huang, X., et al., 2020a. Extension of grouting-induced splitting fractures in materials similar to coal rocks containing prefabricated fractures. J. Geophys. Eng. https://doi.org/10.1093/jge/gxaa021.

Zhang, D., Ranjith, P.G., Perera, M.S.A., 2016. The brittleness indices used in rock mechanics and their application in shale hydraulic fracturing: a review. J. Petrol. Sci. Eng. 143, 158–170. https://doi.org/10.1016/j.petrol.2016.02.011.

Zhang, J., Li, X., Chen, Z., et al., 2019a. Numerical simulation of the improved gas production from low permeability hydrate reservoirs by using an enlarged highly permeable well wall. J. Petrol. Sci. Eng. 183, 106404. https://doi.org/10.1016/j.petrol.2019.106404.

Zhang, W., Shi, X., Jiang, S., et al., 2020b. Experimental study of hydraulic fracture initiation and propagation in highly saturated methane-hydrate-bearing sands. J. Nat. Gas Sci. Eng. 79. https://doi.org/10.1016/j.jngse.2020.103338.

Zhang, Y., Ma, Y., Hu, Z., et al., 2019b. An experimental investigation into the characteristics of hydraulic fracturing and fracture permeability after hydraulic fracturing in granite. Renew. Energy 140, 615–624. https://doi.org/10.1016/j.renene.2019.03.096.

Zhang, Z., Shao, Z., Fang, X., et al., 2018. Research on the fracture grouting mechanism and PFC numerical simulation in loess. Adv. Mater. Sci. Eng. 2018, 1–7. https://doi.org/10.1155/2018/4784762.

Zhu, H., Han, L., Meng, Q., et al., 2021. The split-permeation grouting mechanism of loose and broken coal rock masses considering the temporal and spatial characteristics of slurry viscosity. KSCE J. Civ. Eng. 25 (5), 1887–1900. https://doi.org/10.1007/s12205-021-1715-0.